

# Wave-equation tomography using image-space phase encoded data

Claudio Guerra \*, Yaxun Tang, and Biondo Biondi, Stanford University

## SUMMARY

We present the image-space wave-equation tomography to the generalized source domain, where a smaller number of synthesized shot gathers are generated. Specifically, we generate synthesized shot gathers by image-space phase encoding. The comparison of the gradients of the tomography objective functional obtained using image-space encoded gathers with that obtained using the original shot gathers shows that those encoded shot gathers can be used in wave-equation tomography problems. The advantages of using image-space encoded data is the decreased computational when compared to that of the original shot gathers and the ability of performing velocity analysis in a target-oriented way. We illustrate our examples on Marmousi model.

## INTRODUCTION

Wave-equation tomography has the potential to accurately estimate the velocity model in complex geological scenarios where ray-based traveltome tomography is prone to fail. That is because wave-equation tomography uses band-limited wavefields instead of infinite-frequency rays as carriers of information, thus it is robust even in the presence of strong velocity contrasts and immune from multi-pathing issues. However, despite its theoretical advantages, wave-equation tomography is still computationally challenging.

Wave-equation tomography can be performed on data-space domain (Tarantola, 1987; Woodward, 1992) or in the image-space domain (Biondi and Sava, 1999; Shen, 2004). The image-space approach minimizes the residual in the image domain obtained after migration. Independently on the domain of application of wave-equation tomography, the use of phase encoded data can substantially decrease the computational cost (Vigh and Starr, 2008; Shen and Symes, 2008). Tang et al. (2008) extended the theory of image-space wave-equation tomography from the conventional shot-profile domain (Shen, 2004) to the generalized source domain. The generalized source domain can be obtained either by data-space phase encoding (Whitmore, 1995; Romero et al., 2000) or image-space phase encoding (Guerra and Biondi, 2008). Image-space phase encoding is used to combine data synthesized by the prestack exploding-reflector model (Biondi, 2006, 2007). The prestack exploding-reflector model synthesizes data and the corresponding source function by upward propagating wavefields, having as initial condition a prestack image computed with wave-equation migration.

In this paper, we show that image-space encoded data can provide the gradient of the tomographic objective functional similar to that obtained in the original shot-profile domain, but with less computational cost. We briefly discuss the theory of wave-equation tomography in the image-space domain, then

we explain the prestack exploding-reflector modeling and how the image-space phase encoding can be used to speed up wave-equation tomography in the image domain. We use Marmousi model to illustrate the theory.

## IMAGE-SPACE WAVE-EQUATION TOMOGRAPHY

Image-space wave-equation tomography is a non-linear inverse problem that tries to find an optimal background slowness that minimizes the residual field,  $\Delta\mathbf{I}$ , defined in the image space. The residual field is derived from the background image,  $\mathbf{I}$ , which is computed with a background slowness. The general form of the residual field is (Biondi, 2008)

$$\Delta\mathbf{I} = \mathbf{I} - \mathbf{F}(\mathbf{I}), \quad (1)$$

where  $\mathbf{F}$  is a focusing operator, which measures the focusing of the migrated image. In particular, in the Differential Semblance Optimization (DSO) method (Shen, 2004), the focusing operator takes the form:

$$\mathbf{F}(\mathbf{I}) = (\mathbf{1} - \mathbf{O})\mathbf{I}, \quad (2)$$

where  $\mathbf{1}$  is the identity operator and  $\mathbf{O}$  is the DSO operator either in the subsurface offset domain or in the angle domain (Shen, 2004).

Under  $\ell_2$  norm, the tomography objective function can be written as follows:

$$J = \frac{1}{2} \|\Delta\mathbf{I}\|_2 = \frac{1}{2} \|\mathbf{I} - \mathbf{F}(\mathbf{I})\|_2^2. \quad (3)$$

The gradient of  $J$  with respect to the slowness  $\mathbf{s}$  is

$$\nabla J = \left( \frac{\partial\mathbf{I}}{\partial\mathbf{s}} - \frac{\partial\mathbf{F}(\mathbf{I})}{\partial\mathbf{s}} \right)^* (\mathbf{I} - \mathbf{F}(\mathbf{I})), \quad (4)$$

where  $*$  denotes the adjoint.

The adjoint of the linear operator  $\left. \frac{\partial\mathbf{I}}{\partial\mathbf{s}} \right|_{\mathbf{s}=\hat{\mathbf{s}}}$ , which defines a linear mapping from the slowness perturbation  $\Delta\mathbf{s}$  to the image perturbation  $\Delta\mathbf{I}$ , can be computed by expanding the image  $\mathbf{I}$  around the background slowness  $\hat{\mathbf{s}}$ . Keeping only the zero and first order terms, we get the linear operator  $\left. \frac{\partial\mathbf{I}}{\partial\mathbf{s}} \right|_{\mathbf{s}=\hat{\mathbf{s}}}$  as follows:

$$\Delta\mathbf{I} = \left. \frac{\partial\mathbf{I}}{\partial\mathbf{s}} \right|_{\mathbf{s}=\hat{\mathbf{s}}} \Delta\mathbf{s} = \mathbf{T}\Delta\mathbf{s}, \quad (5)$$

where  $\Delta\mathbf{I} = \mathbf{I} - \hat{\mathbf{I}}$ ,  $\hat{\mathbf{I}}$  is the background image computed with the background slowness  $\hat{\mathbf{s}}$  and  $\Delta\mathbf{s} = \mathbf{s} - \hat{\mathbf{s}}$ .  $\mathbf{T} = \left. \frac{\partial\mathbf{I}}{\partial\mathbf{s}} \right|_{\mathbf{s}=\hat{\mathbf{s}}}$  is the wave-equation tomographic operator. The tomographic operator can be evaluated either in the source and receiver domain (Sava, 2004) or in the shot-profile domain (Shen, 2004).

In the shot-profile domain, both source and receiver wavefields are downward continued with the one-way wave equation (Claerbout, 1971) and the image is computed by applying

## Image-space wave-equation tomography

the cross-correlation imaging condition:

$$I(\mathbf{x}, \mathbf{h}) = \sum_{\mathbf{x}_s} \sum_{\omega} D(\mathbf{x} - \mathbf{h}, \mathbf{x}_s, \omega) U(\mathbf{x} + \mathbf{h}, \mathbf{x}_s, \omega), \quad (6)$$

where  $D(\mathbf{x}, \mathbf{x}_s, \omega)$  is the source wavefield for a single frequency  $\omega$  at image point  $\mathbf{x} = (x, y, z)$  with the source located at  $\mathbf{x}_s = (x_s, y_s, 0)$ ;  $U(\mathbf{x}, \mathbf{x}_s, \omega)$  is the receiver wavefield;  $\mathbf{h} = (h_x, h_y, h_z)$  is the subsurface half offset.

The perturbed image can be derived by the application of the chain rule to Equation 6:

$$\Delta I(\mathbf{x}, \mathbf{h}) = \sum_{\mathbf{x}_s} \sum_{\omega} (\Delta D(\mathbf{x} - \mathbf{h}, \mathbf{x}_s, \omega) \widehat{U}(\mathbf{x} + \mathbf{h}, \mathbf{x}_s, \omega) + \widehat{D}(\mathbf{x} - \mathbf{h}, \mathbf{x}_s, \omega) \Delta U(\mathbf{x} + \mathbf{h}, \mathbf{x}_s, \omega)), \quad (7)$$

where  $\widehat{D}(\mathbf{x} - \mathbf{h}, \mathbf{x}_s, \omega)$  and  $\widehat{U}(\mathbf{x} + \mathbf{h}, \mathbf{x}_s, \omega)$  are the background source and receiver wavefields computed with the background slowness  $\widehat{s}(\mathbf{x})$ ;  $\Delta D(\mathbf{x} - \mathbf{h}, \mathbf{x}_s, \omega)$  and  $\Delta U(\mathbf{x} + \mathbf{h}, \mathbf{x}_s, \omega)$  are the perturbed source wavefield and perturbed receiver wavefield, which are the results of the slowness perturbation  $\Delta s(\mathbf{x})$ . The perturbed source and receiver wavefields satisfy the perturbed one-way wave equation (Shen, 2004).

To evaluate the adjoint tomographic operator  $\mathbf{T}^*$ , we first apply the adjoint of the imaging condition in Equation 7 to get the perturbed source and receiver wavefields  $\Delta D(\mathbf{x}, \mathbf{x}_s, \omega)$  and  $\Delta U(\mathbf{x}, \mathbf{x}_s, \omega)$  as follows:

$$\Delta D(\mathbf{x}, \mathbf{x}_s, \omega) = \sum_{\mathbf{h}} \Delta I(\mathbf{x}, \mathbf{h}) \overline{\widehat{U}(\mathbf{x} + \mathbf{h}, \mathbf{x}_s, \omega)}, \quad (8)$$

$$\Delta U(\mathbf{x}, \mathbf{x}_s, \omega) = \sum_{\mathbf{h}} \Delta I(\mathbf{x}, \mathbf{h}) \overline{\widehat{D}(\mathbf{x} - \mathbf{h}, \mathbf{x}_s, \omega)}. \quad (9)$$

Then we solve the adjoint perturbed one-way wave equation to get the slowness perturbation  $\Delta s(\mathbf{x})$  (Shen, 2004). More detailed information on how to evaluate the forward and adjoint operators can be found in Tang et al. (2008).

### PRESTACK EXPLODING-REFLECTOR MODELING

The general idea of the prestack exploding-reflector modeling (Biondi, 2006) is to model the data and the corresponding source function that are related to only one event in the subsurface. In this case, a single unfocused subsurface-offset-domain common-image gather (SODCIG) containing a single reflector is used as the initial condition for the recursive upward continuation with the following one-way wave equations:

$$\begin{cases} \left( \frac{\partial}{\partial z} - i\Lambda \right) \widetilde{Q}_D(\mathbf{x}, \omega; x_m, y_m) = I_D(\mathbf{x}, \mathbf{h}; x_m, y_m) \\ \widetilde{Q}_D(x, y, z = z_{\max}, \omega; x_m, y_m) = 0 \end{cases}, \quad (10)$$

and

$$\begin{cases} \left( \frac{\partial}{\partial z} - i\Lambda \right) \widetilde{Q}_U(\mathbf{x}, \omega; x_m, y_m) = I_U(\mathbf{x}, \mathbf{h}; x_m, y_m) \\ \widetilde{Q}_U(x, y, z = z_{\max}, \omega; x_m, y_m) = 0 \end{cases}, \quad (11)$$

where  $I_D(\mathbf{x}, \mathbf{h}; x_m, y_m)$  and  $I_U(\mathbf{x}, \mathbf{h}; x_m, y_m)$  are the isolated SODCIGs at the horizontal location  $(x_m, y_m)$  for a single reflector,

and are suitable for the initial conditions for the source and receiver wavefields, respectively. As Biondi (2006) discusses, a rotation of the image gathers according to the apparent geological dip must be performed prior to modeling. By collecting the wavefields at the surface, we obtain the areal source data  $Q_D(x, y, z = 0, \omega; x_m, y_m)$  and the areal receiver data  $Q_U(x, y, z = 0, \omega; x_m, y_m)$  for a single reflector and a single SODCIG located at  $(x_m, y_m)$ .  $\Lambda$  is the square-root operator defined by

$$\Lambda = \sqrt{\omega^2 s^2(\mathbf{x}) - |\mathbf{k}|^2},$$

where  $s(\mathbf{x})$  is the slowness at  $\mathbf{x}$ ;  $\mathbf{k} = (k_x, k_y)$  is the spatial wavenumber vector.

Since the size of the migrated image volume can be very big in practice and there are usually many reflectors in the subsurface, modeling each reflector and each SODCIG may generate a data set even bigger than the original data set. One strategy to reduce the cost is to model several reflectors and several SODCIGs simultaneously (Biondi, 2006); however, this process generates unwanted crosstalk. As discussed by Guerra and Biondi (2008), random phase encoding could be used to attenuate the crosstalk.

### IMAGE-SPACE PHASE ENCODED WAVEFIELDS

The randomly encoded areal source and areal receiver wavefields can be computed as follows:

$$\begin{cases} \left( \frac{\partial}{\partial z} - i\Lambda \right) \widetilde{Q}_D(\mathbf{x}, \mathbf{p}_m, \omega) = \widetilde{I}_D(\mathbf{x}, \mathbf{h}, \mathbf{p}_m, \omega) \\ \widetilde{Q}_D(x, y, z = z_{\max}, \mathbf{p}_m, \omega) = 0 \end{cases}, \quad (12)$$

and

$$\begin{cases} \left( \frac{\partial}{\partial z} - i\Lambda \right) \widetilde{Q}_U(\mathbf{x}, \mathbf{p}_m, \omega) = \widetilde{I}_U(\mathbf{x}, \mathbf{h}, \mathbf{p}_m, \omega) \\ \widetilde{Q}_U(x, y, z = z_{\max}, \mathbf{p}_m, \omega) = 0 \end{cases}, \quad (13)$$

where  $\widetilde{I}_D(\mathbf{x}, \mathbf{h}, \mathbf{p}_m, \omega)$  and  $\widetilde{I}_U(\mathbf{x}, \mathbf{h}, \mathbf{p}_m, \omega)$  are the encoded SODCIGs. They are defined as:

$$\begin{aligned} \widetilde{I}_D(\mathbf{x}, \mathbf{h}, \mathbf{p}_m, \omega) &= \sum_{x_m, y_m} I_D(\mathbf{x}, \mathbf{h}, x_m, y_m) \beta, \\ \widetilde{I}_U(\mathbf{x}, \mathbf{h}, \mathbf{p}_m, \omega) &= \sum_{x_m, y_m} I_U(\mathbf{x}, \mathbf{h}, x_m, y_m) \beta, \end{aligned} \quad (14)$$

where  $\beta = e^{i\gamma(\mathbf{x}, x_m, y_m, \mathbf{p}_m, \omega)}$  is chosen to be the random phase-encoding function, with  $\gamma(\mathbf{x}, x_m, y_m, \mathbf{p}_m, \omega)$  being a uniformly distributed random sequence in  $\mathbf{x}$ ,  $x_m$ ,  $y_m$  and  $\omega$ ; the variable  $\mathbf{p}_m$  is the index of different realizations of the random sequence. Recursively solving Equations 12 and 13 gives us the encoded areal source data  $\widetilde{Q}_D(x, y, z = 0, \mathbf{p}_m, \omega)$  and encoded areal receiver data  $\widetilde{Q}_U(x, y, z = 0, \mathbf{p}_m, \omega)$ , which can be collected at any depth level.

In the image-space wave-equation tomography, the image-space encoded areal data sets are downward continued using the one-way wave equation. The image is produced by cross-correlating the two wavefields and summing images for all realizations  $\mathbf{p}_m$ , as follows:

$$I_{\text{me}}(\mathbf{x}, \mathbf{h}) = \sum_{\mathbf{p}_m, \omega} \widetilde{D}(\mathbf{x}, \mathbf{p}_m, \omega) \widetilde{U}(\mathbf{x}, \mathbf{p}_m, \omega). \quad (15)$$

The initial condition for modeling simultaneous events is set by regularly selecting SODCIGs in the prestack image. Due

## Image-space wave-equation tomography

to the localized nature of the initial conditions used to model prestack exploding reflector data, the amount of crosstalk in the image  $I_{me}(\mathbf{x}, \mathbf{h})$  can be controlled by conveniently choosing the sampling interval of SODCIGs used simultaneously for the modeling. For the case of one reflector, if the SODCIG interval is greater than twice the maximum subsurface offset of the prestack image, no crosstalk is generated.

The perturbed image is obtained by applying chain rule on Equation 15. The slowness perturbation is computed by applying the adjoint of the tomographic operator,  $\mathbf{T}^*$ , to the image perturbation.

### NUMERICAL EXAMPLES

We test the image-space wave-equation tomography using image-space encoded data on a smoothed version of the Marmousi model, computed by applying a 200m 2D-median filter on the slowness model. One-way data were synthesized considering a reflectivity computed from the Marmousi stratigraphic velocity model. We modeled 376 shots, ranging from 0 to 9000m, at every 24m. We used split-spread acquisition geometry, with maximum offset of 6600m and receiver spacing of 24m.

Figure 1(a) shows the slowness model. The background velocity model is equal to the correct velocity model above 2400m depth and the anticlinal with apex at  $(x = 6000m, z = 1850m)$ . Therefore, the slowness perturbation is zero in this portion of the model. Below these horizons, the background model is characterized by a smoother version of the original Marmousi model, computed with a 400m 2D-median filter and scaled down by a factor of 5%. Figure 1(b) shows the slowness perturbation computed by taking the difference between the correct and the background slowness. To compute the image-space

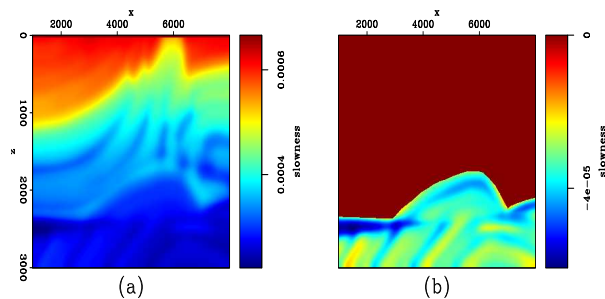


Figure 1: a) Correct slowness; b) Slowness perturbation.

encoded data, we picked 8 reflectors in the non-zero slowness perturbation part, on the prestack image computed with the 376 original shots using the background slowness model. Figure 2 shows the background image (Figure 2a) computed with shot-profile migration and the windowed data (Figure 2b) used as initial condition for the image-space encoded data. Two image-space encoded data were synthesized with different parameters. For both, just one random realization per areal shot was generated. One contains areal shots initiated simultaneously at every 11 CMP positions and encoded according to the CMP position and reflector number, originating 11 areal

shot gathers. The other dataset was modeled having SODCIG sampling interval of 31, or 744m. Given that the SODCIG sampling interval is greater than twice the maximum subsurface offset, 720m, the second data is expected to generate less crosstalk. Figure 3 shows the image perturbation computed

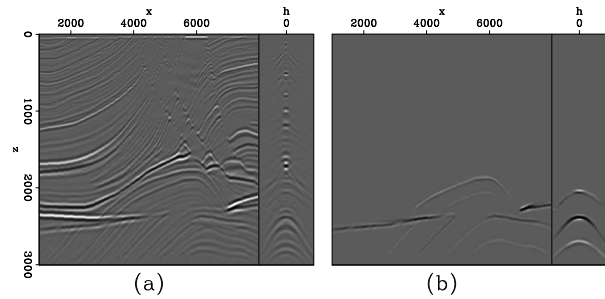


Figure 2: a) Background image; b) Windowed image used to compute image-space encoded data.

by applying the forward tomographic operator,  $\mathbf{T}$ , and using the background slowness and the known slowness perturbation of Figure 1b. The panel on the left corresponds to the zero-subsurface offset section and the panel on the right is the SODCIG at CMP position 6500m. Figure 3a shows the image perturbation computed in the shot-profile domain for the 376 shots; Figure 3b shows the image perturbation computed in the image-space encoded domain using 11 image-space encoded gathers; and Figure 3c shows the image perturbation computed in the image-space encoded domain using 31 image-space encoded gathers. Notice that the dispersed crosstalk is stronger in Figure 3b than in Figure 3c.

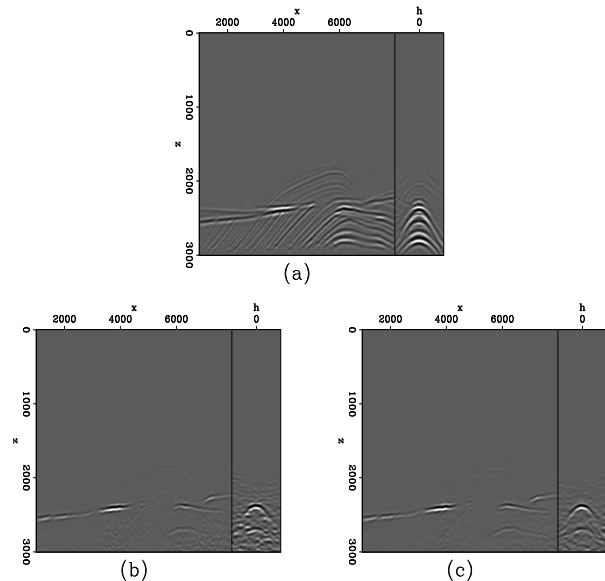


Figure 3: a) Image perturbation in the shot-profile domain; b) Image perturbation computed with 11 image-space encoded wavefields; c) Image perturbation computed with 31 image-space encoded wavefields.

## Image-space wave-equation tomography

Figure 4 illustrates the predicted slowness perturbations by applying the adjoint tomographic operator  $\mathbf{T}^*$  to the image perturbations of Figure 3. Compare with the correct slowness perturbation of Figure 1(b). Figure 4a is the predicted slowness perturbation by back-projecting Figure 3a using all 376 shot gathers; Figure 4b refers to the by back-projection of Figure 3b using 11 image-space encoded gathers; and Figure 4c shows the back-projection of Figure 3c using 31 image-space encoded gathers. The predicted slowness perturbation with image-space encoded gathers, in general, shows a similar structure to that obtained with the original shot gathers. The differences can be credited, at first order, to a sub-optimal number of selected reflectors for the prestack exploding reflector modeling. It is possible that, by selecting more reflectors, we can decrease this difference. In addition, in spite of the stronger crosstalk residual in the image perturbation for the 11 image-space encoded gathers, the predicted slowness perturbation is very similar for the image-space encoded data. Finally, in Figure 5, we show the gradients of the DSO ob-

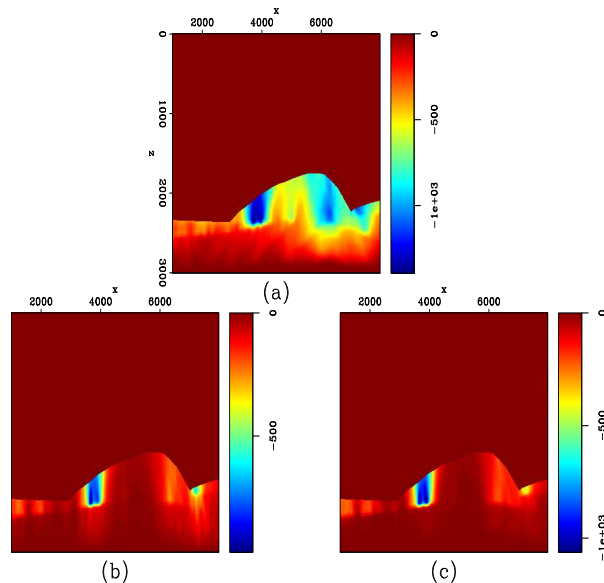


Figure 4: Slowness perturbation obtained by applying the adjoint tomographic operator  $\mathbf{T}^*$  on the image perturbations in Figure 3. a) slowness perturbation computed from Figure 3a; b) slowness perturbation computed from Figure 3b; c) slowness perturbation computed from Figure 3c.

jective function computed by back-projecting the image perturbation computed with DSO. Figure 5a is the DSO gradient obtained in the original shot-profile domain, using 376 shots; Figure 5b shows the DSO gradient computed with 11 image-space encoded wavefields, and Figure 5c shows the DSO gradient computed with 31 image-space encoded wavefields. Even though the DSO gradient computed with image-space phase encoded wavefields is less well behaved than that of the shot-profile domain, it is important to notice that, the gradient is pointing towards the correct direction, which is crucial for a gradient-based optimization algorithm to converge to the correct solution.

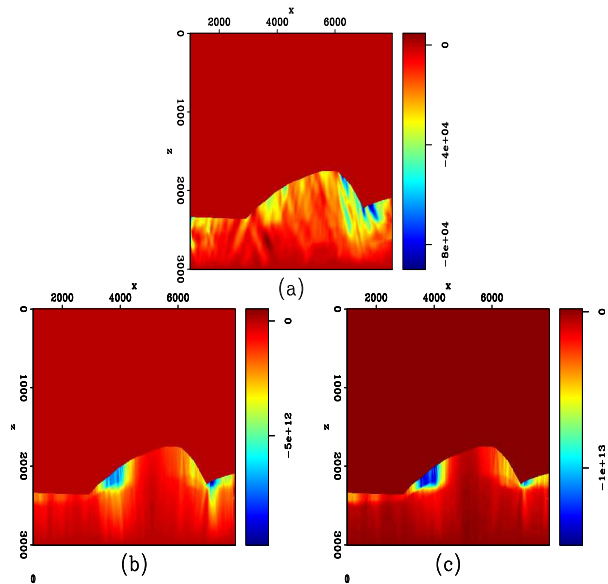


Figure 5: Gradients of the DSO objective function. a) using 376 original gathers; b) using 11 image-space encoded wavefields; c) using 31 image-space encoded wavefields.

## CONCLUSIONS

We presented a cost effective method to perform image-space wave-equation tomography using image-space phase-encoded shot gathers. One important advantage is that we are able to synthesize a much smaller data set while still keeping necessary velocity information for migration velocity analysis; hence the computational cost of performing image-space wave-equation tomography can be significantly reduced. Our results show that using the image-space phase encoded wavefields, provide a gradient of the tomography objective functional similar to that computed using the original shot gathers, but at significantly lower cost. The correct gradient is thus important for the gradient-based optimization algorithm to converge to the correct solution.

## ACKNOWLEDGMENTS

The authors would like to thank the sponsors of the Stanford Exploration Project for their financial support.

## EDITED REFERENCES

Note: This reference list is a copy-edited version of the reference list submitted by the author. Reference lists for the 2009 SEG Technical Program Expanded Abstracts have been copy edited so that references provided with the online metadata for each paper will achieve a high degree of linking to cited sources that appear on the Web.

## REFERENCES

- Biondi, B., 2006, Prestack exploding-reflectors modeling for migration velocity analysis: 76th Annual International Meeting, SEG, Expanded Abstracts, 3056–3060.
- Biondi, B., 2007, Prestack modeling of image events for migration velocity analysis: SEP-131, 101–118.
- Biondi, B., 2008, Automatic wave-equation migration velocity analysis: SEP-134, 65–78.
- Biondi, B. and P. Sava, 1999, Wave-equation migration velocity analysis: 69th Annual International Meeting, SEG, Expanded Abstracts, 1723–1726.
- Claerbout, J. F., 1971, Towards a uni?ed theory of re?ector mapping: *Geophysics*, 36, 467–481.
- Guerra, C. and B. Biondi, 2008, Prestack exploding reflector modeling: The crosstalk problem: SEP-134, 79–92.
- Romero, L. A., D. C. Ghiglia, C. C. Ober, and S. A. Morton, 2000, Phase encoding of shot records in prestack migration: *Geophysics*, 65, 426–436.
- Sava, P., 2004, Migration and velocity analysis by wavefield extrapolation: Ph.D. thesis, Stanford University.
- Shen, P., 2004, Wave-equation migration velocity analysis by differential semblance optimization: Ph.D. thesis, Rice University.
- Shen, P., and W. W. Symes, 2008, Automatic velocity analysis via shot profile migration: *Geophysics*, 73, no. 5, VE49–VE59.
- Tang, Y., C. Guerra, and B. Biondi, 2008, Image-space wave-equation tomography in the generalized source domain: SEP-136, 1–22.
- Tarantola, A., 1987, *Inverse problem theory: Methods for data fitting and model parameter estimation*: Elsevier.
- Vigh, D. and E. W. Starr, 2008, 3d prestack plane-wave, full-waveform inversion: *Geophysics*, 73, no. 5, VE135–VE144.
- Whitmore, N. D., 1995, An imaging hierarchy for common angle plane wave seismogram: Ph.D. thesis, University of Tulsa.
- Woodward, M. J., 1992, Wave-equation tomography: *Geophysics*, 57, 15–26.